PCCP

Accepted Manuscript

ROYAL SOCIETY OF CHEMISTRY

www.rsc.org/pccp

Physical Chemistry
Chemical Physics

RSCPublishing

ARTICLE

Tunable thermodynamic stability of Au−CuPt core−shell trimetallic nanoparticles by controlling alloy composition: Insights from atomistic simulations

Cite this: DOI: 10.1039/x0xx00000x

Received 00th June 2014,
Accepted 00th June 2014

DOI: 10.1039/x0xx00000x

www.rsc.org/

Rao Huang,[a] Gui-Fang Shao,[b] Yu-Hua Wen,[*,a] and Shi-Gang Sun [c]

Microscopic understanding of thermal stability of metallic core-shell nanoparticles is of importance for their synthesis and ultimate application in catalysis. In this article, molecular dynamics simulations have been employed to investigate the thermodynamic evolution of Au-CuPt core-shell trimetallic nanoparticles with various Cu/Pt ratios during heating process. Our results show that the thermodynamic stability of these nanoparticles has remarkably enhanced with rising Pt compositions in CuPt shell. The melting of the nanoparticles all initiates at surface and gradually spreads into the core. Due to the lattice mismatch among Au, Cu and Pt, stacking faults have been observed in the shell and their numbers are associated with Cu/Pt ratio. With the increased temperature, they have continuously reduced for Cu-dominated shell while more stacking faults have been produced for Pt-dominated shell because of significantly different thermal expansion coefficients of the three metals. Beyond the overall melting, all nanoparticles have transformed into trimetallic mixing alloy coated by Au-dominated surface. This work provides a fundamental perspective on the thermodynamic behaviors of trimetallic even multimetallic nanoparticles at atomistic level, indicating that controlling the alloy composition is an effective strategy to realize tunable thermal stability of metallic nanocatalysts.

1. Introduction

Nano-sized particles of noble metals Pt, Pd, Au, and Ru are of increasing significance for modern society because of their usages as indispensable catalysts in chemical industries, environmental protection, and new-energy resources such as fuel cells and lithium ion batteries.[1-3] Due to the rare reserve on the earth and high cost of these metals, improving their catalytic activity and utilization efficiency therefore becomes a grand challenge that emerges for their practical applications. Considering that catalytic reactions usually occur on the surface of nanoparticles (NPs), there are two main ways to reduce these precious metal loadings and to maximize the efficiency in their uses. One way is to enhance their surface-to-volume ratios by synthesizing smaller particles.[4,5] However, both the chemical and thermal stabilities of smaller NPs become worse [6,7] and their structures may be transformed from crystal to noncrystal with reducing particle size [8], which is disadvantageous to the catalytic reactions. The other way is to prepare the NPs with high-index facets because high-index planes possess great density of low-coordinated atoms situated on steps, ledges, and kinks.[3,9] A representative example is that tetrahexahedral Pt NPs bounded by {730} and vicinal high-index facets, have exhibited a significantly enhancing catalytic activity.[10,11] However, due to the high surface energy of the NPs, these high-index-faceted surface structures are more easily destroyed at elevated temperature compared with low-index-faceted ones [12,13], resulting in the vanishing of their excellent catalytic properties.

Besides the aforementioned two ways, synthesis of bimetallic and multimetallic NPs, as the third strategy, has attracted growing attention because their catalytic properties are considerably sensitive to their compositions.[1,14-16] This way can remarkably decrease the cost of metallic catalysts by selectively introducing a cheap metal into noble ones.[17] More importantly, it exhibits an attractive perspective for effectively tuning the functionalities of metallic nanocatalysts by controlling their architectures and compositions, and ultimately realizing the bifunctional even multifunctional catalytic activity owing to the synergy effect of electronic structures of different metals.[16] According to the distributions of elemental compositions, bimetallic and multimetallic NPs may be classified into core-

shell and alloyed structures.[14-18] Among these NPs, Au-Pt bimetallic NPs are particularly interesting due to their excellent catalytic activities. For example, Au-Pt core-shell NPs exhibit enhancing CO tolerance for hydrogen activation [19], and higher electrocatalytic activity for both methanol oxidation reaction (MOR) and oxygen reduction reaction (ORR) than Pt monometallic catalysts [20,21]. On this basis, the third metal has been introduced into the Au-Pt core-shell systems to form trimetallic NPs. For instance, Au@Pd@Pt triple-layered core-shell NPs, consisting of Au inner core, Pd intermediate layer, and Pt outer shell, have been successfully synthesized by a one-step route.[22] Recently, Cu element have been introduced into Au-Pt system to synthesize the Au-CuPt core-shell NPs by a seed-mediated growth method.[23] Their studies have verified that these Au-CuPt NPs exhibit promising dual catalysis for both ORR and MOR owing to the CuPt alloy effect and core/shell interactions. Moreover, the existence of Au core and Cu alloying not only minimizes the Pt usage but also improves the chemical stability of the Au-CuPt core-shell NPs for fuel cell reactions.

As is mentioned above, the core-shell NPs, in which the core and the shell are composed of different elements, respectively, have received a great deal of interest because their properties are remarkably different from those of monometallic counterparts. It is well-known that the thermal stability of metallic NP catalysts is of fundamental significance for their synthesis and final utility owing to the following two reasons: On one hand, the NPs have the trend of aggregating into larger particles because of the enhanced atomic diffusion with the increasing ambient temperature to the Tammann temperature.[24] Thus, to reasonably control the synthesis and catalytic temperature is of technological significance for suppressing the sintering and coarsening of metallic NPs. On the other hand, the catalytic reactions preferentially occur on surface, thereby the surface structures of NPs will play critical roles during the catalytic processes.[3] For example, the catalytic activity can arise from molten structures of nanoparticles under a sonication treatment since coodinatively unsaturated gold atoms increase.[25] Furthermore, composition distribution may be changeable with temperatures due to the differences of alloy elements in cohesive energy, surface energy, atomic radius and diffusivity.[18] Especially, some of catalytic reactions, such as the catalytic cracking of petroleum and the purification of automobile exhaust gases, usually happen in high-temperature environment. Hence, the examination on thermodynamic stability of core-shell NPs is also considerably helpful not only for suppressing their sintering and coarsening but also for investigation on their structure dependent catalytic performances at elevated temperatures.

In this article, we have investigated the thermodynamic stability of Au-CuPt core-shell trimetallic NPs. The reason that the Au-CuPt systems have been chosen is not only because they are promising catalysts [23] but also because Au, Cu and Pt all belong to face-centered cubic (fcc) metals and have moderate differences in both lattice constants and melting points [26]. Different Cu/Pt ratios have been considered in modeling the trimetallic NPs to trace the effects of compositions. Molecular dynamics (MD) simulations were employed to provide insights into the melting behavior and structural evolution of the NPs under continuously heating at atomistic level. Although there have been previous reports on structure and thermal behaviors of ternary alloy clusters,[27,28] these alloy clusters are remarkably smaller than the experimentally synthesized ones, and their structures are significantly different from those of the latter. In this article, both the structures and sizes of NPs were modeled based on the experimental characterization. The article is organized as follows. A brief description of the simulation methodology is given in the following section. Section 3 presents the calculated results, discussion and comparison with available results. The main conclusions are summarized in the fourth section.

2. Simulation Methodology

In order to be reasonably consistent with the experimentally observed structure, Au-CuPt core-shell NPs were constructed from a large fcc single crystal. In modeling the Au-CuPt trimetallic NPs, Au core and CuPt shell are coherent by sharing the same fcc lattice. Initially, Cu and Pt atoms are arbitrarily distributed in the shell by computer-produced random seeds. As an example, Fig. 1 shows the schematic illustration of Au-CuPt core-shell NPs and the corresponding cross-section structures with Cu/Pt atomic ratio equal to one. To investigate the effects of Cu/Pt ratio on the thermodynamic stability, the Pt composition in the shell is continuously varied from 0 to 100% with an increment of 9% or so. Note that the Au-CuPt core-shell NP will be evolved into the Au-Cu one for Pt percentage of zero and the Au-Pt one for Pt percentage of 100%. To facilitate a comparison study, Au, Cu, Pt monometallic and CuPt alloy NPs were also considered in this work. Due to the limitation of our computer facilities available, the total number of atoms was set to be 13 835 for all the modeled NPs, corresponding to the particle radius of 3.7 nm or so. Furthermore, the sizes of Au core were equal for all the Au-CuPt core-shell NPs, and the number of atoms in the core was 4 189.

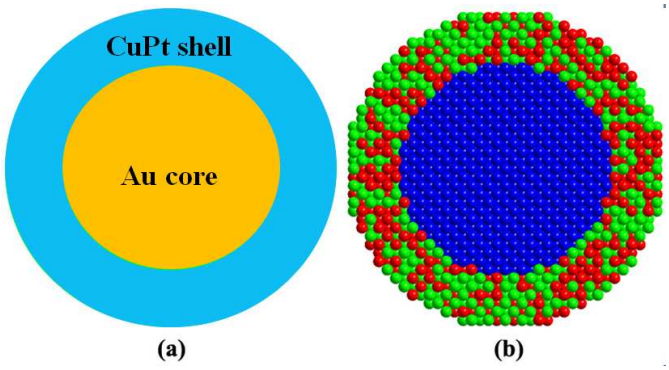

Fig. 1. (a) Schematic illustration for cross-section of Au-CuPt NPs and (b) the corresponding atomic arrangement. Coloring denotes type of atom: blue, Au atom; red, Cu atom; green, Pt atom.

In this study, we employed the quantum corrected Sutton-Chen (Q-SC) type many-body potentials to describe the interatomic interactions.[29] These potentials have been previously used in many studies of fcc metallic nanoparticles and nanowires, demonstrating an accurate description of thermodynamic and mechanical properties.[30-32] According to the framework of the Q-SC potentials, the total energy for a system of atoms can be written as

$$U = \sum_i U_i = \sum_i \varepsilon \left[\frac{1}{2} \sum_{j \neq i} V(R_{ij}) - c\sqrt{\rho_i} \right], \qquad (1)$$

in which $V(R_{ij})$ is a pair interaction function defined by the following equation

$$V(R_{ij}) = \left(\frac{a}{R_{ij}} \right)^n, \qquad (2)$$

accounting for the repulsion between the i and j atomic cores; ρ_i is a local electron density accounting for cohesion associated with atom i defined by

$$\rho_i = \sum_{j \neq i} \left(\frac{a}{R_{ij}} \right)^m . \qquad (3)$$

In Eqs. (1)–(3), R_{ij} is the distance between atoms i and j; a is a length parameter scaling all spacings (leading to dimensionless V and ρ); c is a dimensionless parameter scaling the attractive terms; ε sets the overall energy scale; n and m are integer parameters such that $n > m$. Given the exponents (n, m), c is determined by the equilibrium lattice parameter, and ε is determined by the total cohesive energy. The model parameters for Au, Cu, and Pt are listed in Table 1. In order to describe the interatomic interaction among them, the geometric mean was used to obtain the energy parameter ε while the arithmetic mean was used for the remaining parameters.[31, 32]

Table 1. Potential parameters used in atomistic simulations for Au-CuPt core-shell NPs.[29]

element	n	m	$\mathcal{E}$ (meV)	c	a (Å)
Au	11	8	7.8052	53.581	4.0651
Cu	10	5	5.7921	84.843	3.6030
Pt	11	7	9.7894	71.336	3.9163

Before starting the MD simulations, all the modeled NPs were first quasi-statically relaxed to a local energy minimization through the conjugate gradients method [33]. Afterwards, MD methods were employed to simulate the continuous heating process of the NPs. To make the simulations more realistic, we employed constant temperature and pressure molecular dynamics (NPT-MD) to allow energy and volume fluctuations, which may be critical to the resulting dynamics. The NPs underwent the heating process consisting of a series of NPT-MD simulations from 0 to 2200 K with a temperature increment of 50 K. However, a smaller step of 10 K was adopted to examine the melting behavior more accurately at around the melting point. The simulations were carried out for 200 ps of the relaxation time at each temperature, and the statistical quantities were obtained in the last 25 ps. The desired temperature and ambient pressure were maintained by Nose-Hoover thermostat [34] and Berendsen approach [35], respectively. The equations of atomic motion were integrated by velocity Verlet algorithm with a femtosecond time step.[36]

3. Results and Discussion

Before discussing the thermal stability, we first present the results of caloric curves of Au-CuPt core-shell NPs. Au-$Cu_{64}Pt_{36}$, Au-$Cu_{50}Pt_{50}$, and Au-$Cu_{35}Pt_{65}$ core-shell NPs have been selected as representatives of Au-CuPt core-shell NPs to demonstrate temperature dependence of potential energy, as shown in Fig. 2. For convenience of comparison, the corresponding results of Au and $Cu_{50}Pt_{50}$ alloy NPs with the same atomic number have also been illustrated in this figure. It is clearly seen that at low temperatures, the potential energy increases almost linearly, followed by an abrupt rising. To identify the critical temperature of solid-liquid phase transition, a general approach is to examine the change in the thermodynamic properties such as total energy and specific heat capacity.[37,38] Note that the specific heat capacity can be deduced from temperature-dependent potential energy according to the following equation [30]

$$C_p(T) = \frac{dU}{dT} + \frac{3}{2} R_{gc} \qquad (4)$$

where U is the potential energy, and R_{gc}=8.314 J/molK.

Due to the absorption of latent heat, the solid-liquid phase transition can be well identified by the abrupt rise of the potential energy and the sharp peak of heat capacity.[38] The melting point T_m, usually defined as the temperature at which the heat capacity reaches its maximum, is 1079, 1050, and 1852 K for Au, Cu, and Pt NPs, respectively. Note that the results of Cu and Pt NPs were not illustrated in Fig. 2 only because their temperature-energy relationships were analogous to that of Au NPs. Evidently, the melting temperatures of the monometallic NPs are all remarkably lower than those of their corresponding bulk counterparts (1338, 1358, and 2045 K for Au, Cu, and Pt bulks, respectively) [26], which should be closely associated with high surface-volume ratio in nano-sized particles and low surface premelting temperature.[18,30,31] For the $Cu_{50}Pt_{50}$ alloy NP, its energy curve is also similar to that of Au NPs (see Fig. 2), and the melting point of 1329 K lies between Cu and Pt NPs. A consistent result has been found in our previous study where the melting points of Pt-Pd alloy NPs fall somewhere between those of the corresponding monometallic NPs, depending on the Pd/Pd molar ratio.[18]

It can be seen from Fig. 2 that, unlike Au and CuPt alloy NPs, Au-CuPt core-shell NPs present significantly decreasing potential energies beyond the melting transition. This should be mainly attributed to the enhancing diffusion of Au, Cu and Pt atoms after the overall melting, which partly lowered the total energy and surface energy of systems (see the detailed analysis in the later section). Correspondingly, a negative heat capacity has been observed in the Au-CuPt core-shell NPs. Furthermore,

only one peak occurs in the heat capacity curves of these NPs, indicating that the melting of the Au-CuPt core-shell NPs were continuously developed and finally completed in a narrow temperature region. Nevertheless, there were two prominent peaks existing in the heat capacity curves of Pt-Pd core-shell NPs, signifying a "two-stage" melting behavior.[39] The discrepancy originates from the constituent elements of core and shell. Generally, "two-stage" melting usually occurs in those core-shell NPs in which the bulk melting point of the core element significantly exceeds that of the shell element (for example, 2045 K for bulk Pt and 1827 K for bulk Pd). Otherwise, only one peak can be observed in the caloric curves of core-shell NPs.

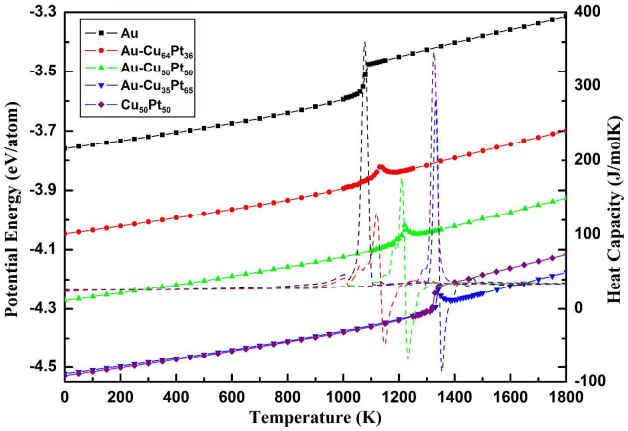

Fig. 2. Dependence of potential energies (solid lines) and the corresponding heat capacities (dashed lines) of Au-CuPt NPs on temperature during continuous heating. The results of Au and CuPt alloy NPs are also displayed for comparison.

Fig. 3 illustrates the melting temperatures of Au-CuPt NPs deduced from their caloric curves. It is evident that the melting points of the Au-CuPt NPs are continuously increased with rising Pt composition in CuPt shell. This progressive increase suggests that the addition of Pt element into the shell can significantly enhance the thermal stability of Au-based NPs. From Fig. 3, two important phenomena should be noted: (i) The melting point of Au-$Cu_{50}Pt_{50}$ core-shell NP is 119 K lower than that of $Cu_{50}Pt_{50}$ alloy NP, indicating that the presence of Au core weakens the thermal stability of CuPt alloy NPs; (ii) The Au-Cu core-shell NP exhibits lower melting point than both Au and Cu NPs. It has been confirmed that the melting temperatures of bimetallic NPs generally lie between those of the corresponding monometallic ones.[18] However, the result of Au-Cu core-shell NPs does not follow this rule. Moreover, the melting point of Au-$Cu_{91}Pt_9$ core-shell NP is also lower than those of Au and Cu NPs, as seen from Fig. 3. These results indicate that there exists a new mechanism determining the melting and associated behaviors of Au-Cu and Au-CuPt core-shell NPs.

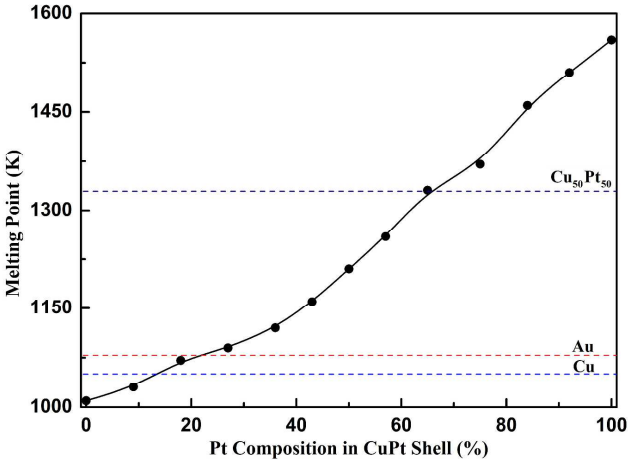

Fig. 3. Dependence of the melting points of Au-CuPt NPs on Pt composition in CuPt shell. Note that the dashed lines correspond to the melting points of monometallic Au, Cu, and Cu-Pt alloy NPs.

Despite the determination of the composition dependent melting points of Au-CuPt core-shell NPs, it is also crucial to further explore the melting behaviors of these NPs with various Cu/Pt ratios. Generally speaking, the melting mechanism of materials can be detected through analyses of the microstructural evolution, root-mean-square displacement of atoms, diffusion coefficients, and so on. Among those methods currently available, the Lindemann index is a simple but effective measurement of thermally driven disorder. It has been frequently used to characterize the thermal evolution of a system.[18,30,31,39] A previous study showed that the Lindemann criterion is well consistent with the Born criterion when examining the onset and evolution of melting.[40] For a system of N atoms, the local Lindemann index for the ith atom in the system is defined as the root-mean-squared bond length fluctuation as [41]

$$\delta_i = \frac{1}{N-1}\sum_{j\neq i}\frac{\sqrt{\langle R_{ij}^2\rangle - \langle R_{ij}\rangle^2}}{\langle R_{ij}\rangle}, \quad (5)$$

and the system-averaged Lindemann index is given by

$$\bar{\delta} = \frac{1}{N}\sum_i \delta_i, \quad (6)$$

where R_{ij} is the distance between the ith and jth atoms. The Lindemann index, based on fluctuations of interatomic distances, provides a sharper criterion for the melting transition in clusters and a clearer separability between solid and liquid phases than that on the basis of the root-mean-squared fluctuations originally introduced by Lindemann.[42] Due to the relaxed constraint of surface atoms, a critical index is around 0.03-0.05 for the melting of clusters or nanoparticles, depending on materials.[42]

Since the critical Lindemann index is dependent on materials, it is necessary for bimetallic or multimetallic particles to separately calculate system-averaged Lindemman index of each element. To ascertain the critical value of Lindemann index during melting, we have calculated the temperature-dependent system-averaged Lindemman indices of monometallic Au, Cu

and Pt NPs with the same atomic number. Similar to the potential energy in Fig. 2, the system-averaged Lindemann indices of Au, Cu and Pt atoms (not shown here) linearly increase with rising temperature before melting and subsequently form a step around the melting point. Afterwards, they resume the close linear dependence of temperature beyond overall melting. According to the melting points of the monometallic NPs, the critical Lindemann index could be appropriately ascertained to be 0.041 for Au, 0.05 for Cu, and 0.043 for Pt, as illustrated by the dash lines in Fig. 4. In order to visualize the melting process and to shed light on the melting mechanism, we have examined the microscopic evolution of Au-CuPt core-shell NPs during continuous heating. Analogous to the study of melting of a surface-free Lennard-Jones crystal,[40] the concept of Lindemann atom has been introduced into this work. In the Lindemann melting criterion, atom whose Lindemann index is larger than its critical value is defined as Lindemann atom. Here we have taken Au-$Cu_{50}Pt_{50}$ core-shell NP as an example to explore the melting mechanism of Au-CuPt core-shell NPs. The snapshots of cross sections at five representative temperatures have been illustrated in Fig. 4 (Up), and the corresponding Lindemann index distributions have been displayed in Fig. 4 (Bottom).

As shown in Fig. 4, the thermodynamic evolution of Au-$Cu_{50}Pt_{50}$ core-shell NP has demonstrated a typical melting process developing from surface into interior, similar to what happen in monometallic NPs [30]. The Au-CuPt core-shell NP can keep its fcc arrangement at low temperatures. The ordered lattice stably retains until 800 K or so. With the temperature increased to 1000 K, Lindemann atoms have emerged on the surface, indicating the initialization of surface melting. It should be noted that the majority of them were Cu atoms, implying the preferential premelting of Cu on the surface. The premelting has enlarged with increasing temperature and expanded over the whole surface at 1200 K (see the second and third snapshots in Fig. 4). Further elevated temperature could make the melting spread into the inner shell even Au core, resulting in the overall melting of Au-CuPt NP at 1220 K, as shown in the fourth snapshot in Fig. 4. Once the melting transition was completed, Au atoms have rapidly diffused into the shell, and the reversed diffusions of Cu and Pt atoms into the core have concomitantly happened, leading to the disappearance of core-shell interfacial structure (see the fourth snapshot and the corresponding Lindemann index distribution in Fig. 4). Further mixing of Au, Cu and Pt atoms has been proceeded with increased temperature and finally formed a typical liquid AuCuPt alloy NP (see the fifth snapshot in Fig. 4). It is worth noting that the outermost layer was dominated by Au atoms in the liquid NP. This aggregative behavior was driven by the minimization of the total energy of alloy NP because Au has remarkably lower surface energy than Cu and Pt [43]. The similar melting process has also been observed in other Au-CuPt core-shell NPs by carefully checking their thermodynamic evolutions under heating process (not illustrated here). The only difference among them is that the increasing Pt composition in CuPt shell elevates the premelting temperatures and the melting points of Au-CuPt core-shell NPs, which is beneficial to enhancing their thermal stability, as indicated by Fig. 3.

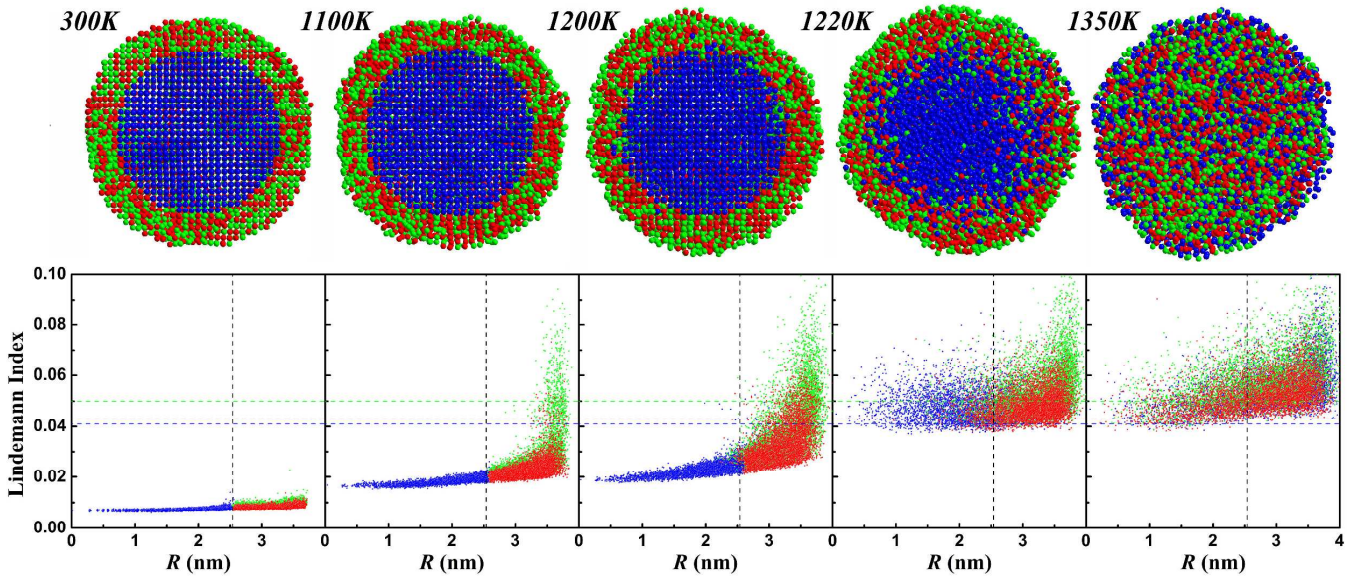

Fig. 4. (Up) Snapshots of cross sections of Au-$Cu_{50}Pt_{50}$ core-shell NP taken at five representative temperatures. Coloring denotes type of atom: blue, Au atom; green, Cu atom; red, Pt atom. (Bottom) Lindemann index distributions of atoms at the corresponding temperatures. Note that the horizontal axis denotes the distance between the atom and the particle center of mass. The vertical dashed line denotes the initial boundary between Au core and CuPt shell while the horizontal ones indicate the critical Lindemann indices: 0.041, 0.05, and 0.043 for Au, Cu and Pt, respectively.

To further characterize the structural evolution of Au-CuPt core-shell NPs under heating process, we have employed the common neighbor analysis (CNA) proposed by Honeycutt and Andersen [44] to identify the local structures in these NPs. The analysis assigns four indices *ijkl* to each pair of atoms which have common neighbors, and provides an accurate description of the local environment of the pair. The CNA method has been successfully used to investigate the structural changes during mechanical deformation and melting process.[45,46] In this analysis, the bonds between an atom and its nearest neighbors are examined to determine the crystal structure. The different types of pairs are associated with different types of local order. All bonded pairs in the fcc crystal are of type 1421, while the hcp crystal has equal numbers of type 1421 and 1422. Considering that for fcc NPs, the pairs beside types of 1421 and 1422 can not reveal any useful information, here we have classified atoms into three categories: Atoms in a local fcc order were considered as fcc atoms; Atoms in a local hcp order were classified as hcp atoms; Atoms in all other local orders were considered to be 'other' atoms. Generally, the occurrence of hcp atoms in fcc crystals signifies the formation of stacking faults which are left behind by the motion of Shockley partial dislocations.[47] Therefore, the use of CNA may make the dislocations and stacking faults visible in atomistic simulations.

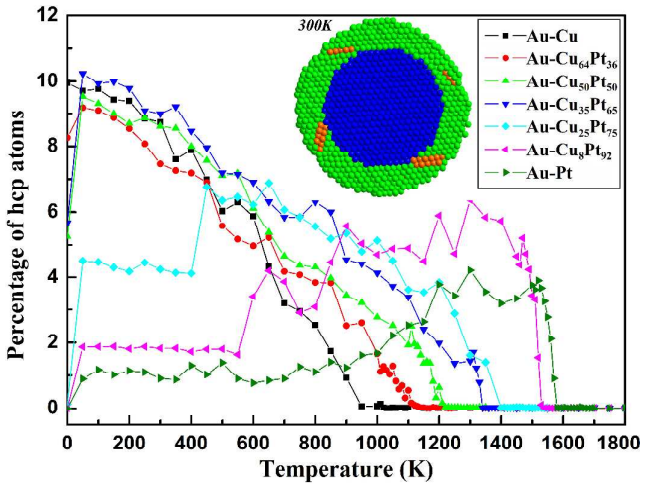

Fig. 5. Percentage of hcp atoms as a function of temperature for Au-CuPt core-shell NPs. (Inset) Snapshot of cross section of Au-$Cu_{50}Pt_{50}$ core-shell NP at 300 K. Coloring denotes atomic type: blue, Au atom; green, Cu or Pt atom; orange, hcp atom.

Fig. 5 shows the temperature-dependent percentages of hcp atoms in Au-CuPt core-shell NPs with different Pt compositions. For Pt composition less than 65%, one can see that there are considerable hcp atoms (above 8% of total atoms) at low temperature (typical lower than 300 K). As a representative, the atomic arrangement of Au-$Cu_{50}Pt_{50}$ core-shell NP at room temperature of 300 K has been inserted into Fig. 5. Evidently, all hcp atoms have been orderly arranged in the CuPt shell, forming a typical structure of stacking faults. No hcp atoms were found in Au core. There hcp atoms have initially appeared after full relaxation at zero temperature and have continuously decreased with increased temperature beyond 50 K. At the melting point, hcp atoms have disappeared and the percentage of 'other' atoms has risen up to 100% or so, indicating the absolute loss of ordered structure and the accomplishment of phase transition to liquid, which is well consistent with the change of the potential energy and the analysis of Lindemann index.

For high Pt composition (typical higher than 75%), a remarkable difference can be observed. As shown in Fig. 5, the initial percentage of hcp atoms strongly depends on the Pt composition. High Pt composition leads to low percentage of hcp atoms in the CuPt shell. Furthermore, the percentage of hcp atoms keeps constant at low temperatures (except 0 K), and the critical temperature is also dependent on Pt composition. With further heating, the number of hcp atoms in the shell has firstly increased, and subsequently decreased to zero until the overall melting. According to the dislocation theory of crystal, an increase in the number of hcp atoms should be attributed to the motion of partial dislocations through the crystal. Therefore, it may be deduced that new dislocations have been initiated with elevated temperatures, leading to the formation of more stacking faults in the shell. Similar to those in the shell of low Pt composition, all hcp atoms finally transform into 'other' atoms after completely melting.

Why does the percentage of hcp atoms exhibit remarkably different dependence on Pt composition of the CuPt shell? This should be closely associated with stress (or strain) distributions in core-shell NPs, which is commonly aroused by the difference lattice parameters and thermal expansion coefficients of elements. In this study, we have calculated the local stress in Au-CuPt core-shell NPs after local energy optimization. Note that the local stress σ_n at the *i*th atom site can be written as

$$\sigma_n = \frac{1}{3}\sum_{\alpha=1}^{3}\sigma_{\alpha\alpha} = \frac{1}{3}\sum_{\alpha=1}^{3}\left(\frac{1}{2\Omega_i}\sum_{j\neq i}F_{ij}^{\alpha}R_{ij}^{\alpha}\right), \quad (7)$$

where F_{ij} and R_{ij} are the force and distance between atoms *i* and *j*. Ω_i is the local volume of the *i*th atom.[48] As a representative, Fig. 6 illustrates the local stress distribution of Au-$Cu_{50}Pt_{50}$ core-shell NP at zero temperature. The average stresses of Au, Cu and Pt atoms are -0.448, 0.004, and 0.268 GPa, respectively, showing that the core is under compressive stress while the shell, on the whole, possesses tensile stress. Furthermore, there exists an observable stress step in the interface between the outer core and inner shell, which should be well correlated with the lattice mismatch at the interface. As we know, the lattice constants are 4.078, 3.615, and 3.924 Å for Au, Cu and Pt, respectively. Due to the larger lattice constant of Au compared with those of Cu and Pt, the lattice of the core will contract after encapsulated by CuPt shell, hence resulting in the compressive stress (or strain) in the core and the tensile stress (or strain) in the shell (see Fig. 6). Furthermore, the stress (or strain) difference between the core

and the shell becomes more remarkable for lower Pt composition because Cu has the smallest lattice constant. To accommodate the stress (or strain) difference in core-shell interface, the Shockley partial dislocations prefer to nucleate in the interface and propagate through the shell, leaving intrinsic stacking faults composed of two adjacent {111} planes of hcp atoms (see the inset in Fig. 5). Just owing to the larger lattice misfit between Au and Cu than that between Au and Pt, the percentage of hcp atoms is generally larger in Au-CuPt core-shell NPs with higher Cu composition at low temperatures, as shown in Fig. 5.

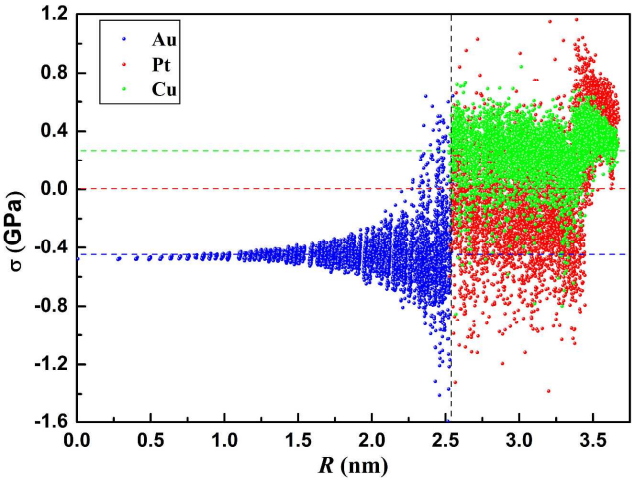

Fig. 6. Distribution of atomic stress as a function of distance of the atom from the particle center of mass. Black dashed line denotes the boundary between the core and the shell, and color one denotes the average stress of the corresponding atoms. Note that the positive value indicates the tensile stress while the negative implies the compressive stress.

Besides the factor of lattice constants, the temperature also affects the stress (or strain) difference between Au core and CuPt shell. It is known that the coefficients of linear thermal expansion are 14.2×10^{-6}, 16.5×10^{-6}, and 8.8×10^{-6} K^{-1} for Au, Cu, and Pt bulks, respectively [49]. As for metallic NP, the thermal expansion coefficient has been experimentally verified to be remarkably higher than that of its bulk counterpart.[50] The thermal expansion coefficient of monometallic NP, calculated from the particle radius versus temperature in our simulations, is 23.97×10^{-6} K^{-1} for Au, 27.26×10^{-6} K^{-1} for Cu, and 12.96×10^{-6} K^{-1} for Pt. The thermal expansion coefficient of CuPt alloy NPs should lies between those of Cu and Pt NPs, depending on the Cu/Pt ratio. For example, it is 18.53×10^{-6} K^{-1} for $Cu_{50}Pt_{50}$ alloy NP. Due to the faster lattice thermal expansion of Au comparing with that of the CuPt shell, the Au core will be subjected to stronger confinement from the CuPt shell during the heating process. Meanwhile, according the thermal expansion coefficients of monometallic NPs, it can be deduced that the Cu shell will expand faster than Au core with rising temperature, therefore decreasing the stress difference at the core-shell interface. As a result, there are few new hcp atoms emerging and the existing hcp atoms will gradually transform into 'other' atoms due to the thermally driven disorder. Therefore, the number of hcp atoms presented a continuous decrease with elevated temperature in the Cu-dominated shell (see Fig. 5). However, the thermal expansion coefficient of CuPt shell is decreased with lowering Cu composition. For Cu composition less than 25%, the shell has been dominated by Pt atoms and its thermal expansion coefficient is distinctly smaller than that of Au core. When the temperature is increased, the stress difference in the core-shell interface will become more significant. The enhanced stress difference will drive more and more partial dislocations to nucleate in the interface and to move through the shell. Resultantly, one can find that the percentage of hcp atoms has presented a continuous rise beyond certain temperature, as indicated by Fig. 5. Nevertheless, all hcp atoms will disappear at the overall melting, and a disorder structure ultimately forms.

Finally, we will elucidate the reason that the melting point of Au-Cu core-shell NP is lower than those of Au and Cu NPs. As is discussed above, the stacking faults have occurred in the Cu shell because of the remarkable lattice misfit in the Au-core/Cu-shell interface. In addition, further structural analysis shows that there exist a larger number of 'other' atoms at the interface and surface. The presence of these defects breaks the initial fcc arrangement of Au-Cu core-shell NP, facilitating the origination of premelting. Actually, the melting process from surface into interior was heterogeneously developed due to the existence of these defects. Therefore, it may be expectable that the Au-Cu core-shell NP has lower melting point than both Au and Cu NPs.

4. Conclusions

In summary, atomistic simulations have been employed to systematically examine the thermodynamic stability of Au-CuPt core-shell trimetallic NPs with tunable Pt compositions from zero to 100%. The Lindemann index and common neighbor analysis have been used to characterize their melting behaviors and structural evolutions during continuous heating. Our results have revealed that the thermodynamic stability of Au-CuPt core-shell NPs is strongly dependent on the Cu/Pt ratios: Their melting points are prominently enhanced with rising Pt compositions of CuPt shell. The atomistic snapshots have demonstrated that for these NPs, the melting processes all start on the surface and gradually propagate into the core. Due to the lattice parameter differences in Au, Cu and Pt, the stacking faults have been observed in the shell, which are usually considered as the production left behind by Shockley partial dislocations. With increasing temperature, these stacking faults have gradually disappeared in Cu-dominated shell while more stacking faults have been formed in Pt-dominated shell because of the remarkable differences in thermal expansion coefficients of Au, Cu and Pt. Both the stacking faults and core-shell interface will be destroyed beyond the overall melting, forming a trimetallic mixing alloy NP coated by Au-dominated surface. These results suggest that the thermodynamic stability of Au-CuPt core-shell NPs can be tunable by controlling the molar ratio of components

in the shell, indicating a highly promising strategy to synthesize core-shell trimetallic even multimetallic NPs with excellent catalytic performance and high stability. The implications of these conclusions are not just limited to Au-Cu-Pt system and could be extrapolated into other trimetallic core-shell NPs. Due to the potential application of core-shell structures in NP catalysts, this study is expected to be of significance not only to the exploitation of trimetallic NPs but also to the further design of multimetallic nanostructures.

Acknowledgements

This work is supported by the National Natural Science Foundation of China (Grant Nos. 51271156 and 11204252), the Natural Science Foundation of Fujian Province of China (Grant No. 2013J06002), and the Specialized Research Fund for the Doctoral Program of Higher Education of China (Grant No. 20130121110012).

Notes and references

* E-mail: yhwen@xmu.edu.cn (Y. H. Wen).
Phone: (+86) 592-218-2248. Fax: (+86) 592-218-9426.
[a] Institute of Theoretical Physics and Astrophysics, Department of Physics, Xiamen University, Xiamen 361005, China
[b] Institute of Pattern Recognition and Intelligent System, Department of Automation, Xiamen University, Xiamen, 361005, China
[c] State Key Laboratory of Physical Chemistry of Solid Surfaces, Department of Chemistry, Xiamen University, Xiamen 361005, China

1 R. Ferrando, J. Jellinek and R. L. Johnston, *Chem. Rev.*, 2008, **108**, 845–910.
2 R. W. Murray, *Chem. Rev.*, 2008, **108**, 2688–2720.
3 Z. Y. Zhou, N. Tian, J. T. Li, I. Broadwell and S. G. Sun, *Chem. Soc. Rev.*, 2011, **40**, 4167–4185.
4 X. C. Zhou, W. L. Xu, G. K. Liu, D. Panda and P. Chen, *J. Am. Chem. Soc.*, 2010, **132**, 138–146.
5 N. Vilar-Vidal, J. Rivas and M. A. Lopez-Quintela, *ACS Catal.*, 2012, **2**, 1693–1697.
6 S. R. Isaacs, H. Choo, W. B. Ko and Y. S. Shon, *Chem. Mater.*, 2006, **18**, 107–114.
7 M. Auffan, J. Rose, M. R. Wiesner and J. Y. Bottero, *Environ. Pollut.*, 2009, **157**, 1127–1133
8 L. Li, L. L. Wang, D. D. Johnson, Z. F. Zhang, S. I. Sanchez, J. H. Kang, R. G. Nuzzo, Q. Wang, A. I. Frenkel, J. Li, J. Ciston, E. A. Stach and J. C. Yang, *J. Am. Chem. Soc.*, 2013, **135**, 13062−13072.
9 N. Tian, Z. Y. Zhou and S. G. Sun, *J. Phys. Chem. C*, 2008, **112**, 19801–19817.
10 N. Tian, Z. Y. Zhou, S. G. Sun, Y. Ding and Z. L. Wang, *Science*, 2007, **316**, 732–735.
11 Z. Y. Zhou, Z. Z. Huang, D. J. Chen, Q. Wang, N. Tian and S. G. Sun, *Angew. Chem. Int. Ed.*, 2010, **49**, 411–414.
12 R. Huang, Y. H. Wen, Z. Z. Zhu and S. G. Sun, *J. Mater. Chem.*, 2011, **21**, 11578–11584.
13 X. M. Zeng, R. Huang, G. F. Shao, Y. H. Wen and S. G. Sun, *J. Mater. Chem. A*, 2014, **2**, 11480–11489.
14 S. Alayoglu, A. U. Nilekar, M. Mavrikakis and B. Eichhorn, *Nature Mater.*, 2008, **7**, 333338.
15 L. Kesavan, R. Tiruvalam, M. H. Ab Rahim, M. I. bin Saiman, D. I. Enache, R. L. Jenkins, N. Dimitratos, J. A. Lopez-Sanchez, S. H. Taylor, D. W. Knight, C. J. Kiely and G. J. Hutchings, *Science*, 2011, **331**, 195–199.
16 S. Khanal, N. Bhattarai, J. J. Velazquez-Salazar, D. Bahena, G. Soldano, A. Ponce, M. M. Mariscal, S. Mejia-Rosalesc and M. Jose-Yacaman, *Nanoscale*, 2013, **5**, 12456–12463.
17 J. H. Jang, E. Lee, J. Park, G. Kim, S. Hong and Y. U. Kwon, *Sci. Rep.*, 2013, **3**, 2872.
18 R. Huang, Y. H. Wen, Z. Z. Zhu and S. G. Sun, *J. Phys. Chem. C*, 2012, **116**, 8664–8671.
19 S. H. Zhou, K. McIlwrath, G. Jackson and B. Eichhorn, *J. Am. Chem. Soc.*, 2006, **128**, 1780–1781.
20 Y. Kim, J. W. Hong, Y. W. Lee, M. Kim, D. Kim, W. S. Yun and S. W. Han, *Angew. Chem. Int. Ed.*, 2010, **49**, 10197−10201.
21 H. Ataee-Esfahani, L. Wang, Y. Nemoto and Y. Yamauchi, *Chem. Mater.*, 2010, **22**, 6310−6318.
22 L. Wang and Y. Yamauchi, *J. Am. Chem. Soc.*, 2010, **132**, 13636–13638.
23 X. L. Sun, D. G. Li, Y. Ding, W. L. Zhu, S. J. Guo, Z. L. Wang and S. H. Sun, *J. Am. Chem. Soc.*, 2014, **136**, 5745–5749.
24 J. M. Sun, D. Ma, H. Zhang, X. M. Liu, X. W. Han, X. H. Bao, G. Weinberg, N. Pfander and D. S. Su, *J. Am. Chem. Soc.*, 2006, **128**, 15756–15764.
25 Y. H. Lee, G. Kim, M. Joe, J. H. Jang, J. Kim, K. R. Lee and Y. U. Kwon, *Chem. Comm.*, 2010, **46**, 5656–5658.
26 C. Kittel, *Introduction to Solid State Physics*, John Wiley & Sons, New York, 1996.
27 A. Aguado and J. M. Lopez, *J. Chem. Theory Comput.*, 2005, **1**, 299–306.
28 A. A. Dzhurakhalov, I. Atanasov and M. Hou, *Phys. Rev. B*, 2008, **77**, 115415.
29 T. Cagin, Y. Kimura, Y. Qi, H. Li, H. Ikeda, W. L. Johnson and W. A. Goddard, *Mater. Res. Soc. Symp. Proc.*, 1998, **554**, 43–48.
30 Y. Qi, T. Cagin, W. L. Johnson and W. A. Goddard, *J. Chem. Phys.*, 2001, **115**, 385–394.
31 S. K. R. S. Sankaranarayanan, V. R. Bhethanabotla and B. Joseph, *Phys. Rev. B*, 2005, **71**, 195415.
32 H. Ikeda, Y. Qi, T. Cagin, K. Samwer, W. L. Johnson and W. A. Goddard, *Phys. Rev. Lett.*, 1999, **82**, 2900–2903.
33 A. R. Leach, *Molecular Modelling: Principles and Applications*, Pearson Education Ltd., London, 2001.
34 D. L. Evans and B. L. Holian, *J. Chem. Phys.*, 1985, **83**, 4069–4074.
35 H. J. C. Berendsen, J. P. M. Postma, W. F. van Gunsteren, A. DiNola and J. R. Haak, *J. Chem. Phys.*, 1984, **81**, 3684–3690.
36 W. C. Swope, H. C. Anderson, P. H. Berens and K. R. Wilson, *J. Chem. Phys.*, 1982, **76**, 637–649.
37 B. Cao, A. K. Starace, O. H. Judd and M. F. Jarrold, *J. Am. Chem. Soc.*, 2009, **131**, 2446−2447.
38 J. Kang, S. H. Wei and Y. H. Kim, *J. Am. Chem. Soc.*, 2010, **132**, 18287−18291.
39 R. Huang, Y. H. Wen, Z. Z. Zhu and S. G. Sun, *J. Phys. Chem. C*, 2012, **116**, 11837−11841.

40 Z. H. Jin, P. Gumbsch, K. Lu and E. Ma, *Phys. Rev. Lett.*, 2001, **87**, 055703.
41 Y. Shibuta and T. Suzuki, *Chem. Phys. Lett.*, 2007, **445**, 265−270.
42 Y. Q. Zhou, M. Karplus, K. D. Ball and R. S. Berry, *J. Chem. Phys.*, 2002, **116**, 2323−2329.
43 Y. N. Wen and H. M. Zhang, *Solid State Commun.*, 2007, **144**, 163–167.
44 J. D. Honeycutt and H. C. Andersen, *J. Phys. Chem.*, 1987, **91**, 4950−4963.
45 J. Schiøtz, F. D. Di Tolla and K. W. Jacobsen, *Nature*, 1998, **391**, 561−563.
46 Y. H. Wen, Y. Zhang, J. C. Zheng, Z. Z. Zhu and S. G. Sun, *J. Phys. Chem. C*, 2009, **113**, 20611–20617
47 J. Schiotz, T. Vegge, F. D. Di Tolla and K. W. Jacobsen, *Phys. Rev. B*, 1999, **60**, 11971–11983.
48 C. Mottet, G. Rossi, F. Baletto and R. Ferrando, *Phys. Rev. Lett.*, 2005, **95**, 035501.
49 A. M. James and M. P. Lord, *Macmillan's Chemical and Physical Data*, Macmillan, London, 1992.
50 W. H. Li, S. Y. Wu, C. C. Yang, S. K. Lai, K. C. Lee, H. L. Huang and H. D. Yang, *Phys. Rev. Lett.*, 2002, **89**, 135504.